

Computational simulation of the relaxation of local stresses due to foreign object damage under cyclic loading

T Davis^a, J Ding^{*a}, W Sun^a and S B Leen^b

^a Department of Mechanical, Materials and Manufacturing Engineering
University of Nottingham, Nottingham NG7 2RD UK

^b College of Engineering and Informatics, National University of Ireland, Galway, Ireland

* Corresponding Author Email: jian.ding@nottingham.ac.uk

Abstract

In this study, the phenomenon of residual stress relaxation from foreign object damage (FOD) is numerically simulated using a hybrid explicit-implicit finite element method. The effects of both low-cycle and high-cycle fatigue loadings on stress relaxation were studied. FOD is first simulated by firing a 3mm cube impacting onto a plate of Ti-6Al-4V at 200m/s. The FOD impact produces two distinct stress concentrations: one is compressive directly beneath the impact site, the other is tensile around the outer edge of the impact. The plate was then assumed to be subjected to a cyclic fatigue loading. The stress relaxation was investigated under a range of stress ratios and maximum applied stresses. Two different material models were considered for the simulations, namely an elastic-perfectly plastic model and a non-linear kinematic hardening model.

Keywords: finite element; impact; foreign object damage (FOD); residual stress; stress relaxation.

Notation

C	material constant
E	Young's modulus
FOD	Foreign Object Damage
HCF	high cycle fatigue
LCF	low cycle fatigue
n	number of load cycles
R	applied stress ratio
R_{local}	local stress ratio
q	material constant
x	backstress tensor
γ	material constant
$\dot{\epsilon}$	strain rate
$\dot{\epsilon}_r$	reference strain rate
$\dot{\epsilon}^{pl}$	plastic strain rate
$\dot{\bar{\epsilon}}^{pl}$	equivalent plastic strain rate
ν	Poisson's ratio
σ_{app}	applied stress
$\Delta\sigma_{app}$	applied stress range
σ_{max}	maximum applied stress
σ_{mean}	mean stress
σ_{min}	minimum applied stress
σ_x	normal stress component in x-direction, i.e. in the direction of applied load
σ_{ys}	yield stress

$\sigma_{ys}(\dot{\epsilon})$ strain rate sensitive yield stress
 σ_y stress component in y-direction
 σ_z stress component in z-direction

1. Introduction

Dynamic impact and subsequent fatigue under cyclic loading conditions demonstrate a very demanding failure mode, which occurs in a number of mechanical applications. Impact leads to either beneficial or detrimental effects on the fatigue performance. For example, the cold working process of shot-peening is used to create a beneficial compressive residual stress field over the surface of the component. This compressive residual stress inhibits surface crack growth and thereby leads to an increase in fatigue life. Spherical shots made from hardened materials are typically used for the shot peening, fired at velocities in the range of 40-100 m/s. [1]. The detrimental effects of impacts are observed in such a phenomenon as Foreign Object Damage (FOD), which occurs primarily during the takeoff and landing periods of aircraft flights, where millimetre sized debris in the form of hard particles such as sand and grit are ingested into aero engines [2-4]. These particles impact the fan and early stage compressor blades, typically made from the titanium alloy Ti-6Al-4V, at speeds in the range of 200 to 350 m/s. Impacts on the leading edge of the blades cause the most severe damage, which is in the form of notch like craters and gives rise to stress concentrations, residual stresses, microcracks around the impact site and distortion of the materials microstructure [3]. The combination of the fatigue loading and the residual stress field induced by the impact can make the impact region a preferential site for both fatigue crack initiation and growth. This reduces the fatigue resistance of the blades and in some cases causes them to fail prematurely. It has been reported that the cost of FOD to both the civil and military aircraft industries is greater than \$4 billion annually [4].

To gain insight into the interaction between FOD and fatigue behaviour, a number of experimental and computational studies have been carried out in the last decade. The FOD was normally simulated experimentally using a gun or ballistic system to fire hardened steel spheres [3-8] or steel cubes [9-11]. Fatigue behaviour due to foreign object damage is a complex topic, which brings together impact mechanics, fracture mechanics and fatigue analysis. A comprehensive predictive methodology was proposed by Chen and Hutchinson [12, 13], in which finite element (FE) analysis was first used to determine the residual stresses and geometric stress concentration due to FOD. Analysis was then carried out to determine when and to what extent the residual stresses and stress concentrations caused by FOD reduce the critical crack size associated with the threshold for fatigue crack growth. More recently, Ding et al [8, 9] studied FOD-induced small crack growth in rolled Ti-6Al-4V plates subjected to combined LCF and HCF loadings, and suggested a two-parameter crack growth model together with a corrected stress intensity solution to correlate the experimental data.

Impact-induced stress is expected to relax under the subsequent fatigue loading. Torres and Voorwald [14] reported significant relaxation of the compressive residual stress field for shot-peened AISI 4340 steel under fatigue loading. The stress relaxation of a Ti-6Al-4V plate subjected to FOD was experimentally investigated by Boyce et al. [15]. It is found that relaxation of both the compressive residual stress beneath the impact and the tensile stress around the edge of the impact, occurred primarily within the first cycle of loading. Compared with experimental studies, numerical simulation of the relaxation and redistribution of the residual stress field after dynamic impact has been so far very scarce. In this context, a hybrid explicit-implicit finite element methodology is developed in this study to simulate the relaxation of the residual stresses induced by FOD. Effects of the maximum applied fatigue stress and the material cyclic hardening behaviour on the relaxation are discussed.

2 Methodology

2.1 Impact modelling

During an impact between two solids, the two energy transformation steps are identified: (i) the phase of deformation where the ‘stream kinetic’ energy is transformed into potential energy of deformation, and (ii) the phase of shot restitution. If the material response is completely elastic, the potential energy is totally transformed into returned kinetic energy. If the response is elastic-plastic, the potential energy is only partially transformed. Considering an impact of a foreign object on a plate that produces both elastic and plastic deformations, only a partial transformation of the potential energy from the impact to kinetic energy will occur. For the case of a normal impact, a coefficient of restitution (e_r) can be given by:

$$e_r = \frac{V_r}{V_i} \quad (1)$$

where V_i is the initial impact velocity and V_r is the returning velocity; e_r takes a value between 0 and 1 for an elastic-plastic impact [16].

In this study the foreign object is assumed to be perfectly rigid, so that it cannot store any plastic deformation. The energy required to cause the plastic deformation of the plate (W_p) is given by:

$$W_p = K\Delta W_\alpha = \frac{1}{2}mV_i^2(1 - e_r^2)K \quad (2)$$

where, the introduction of the efficiency coefficient K is used to account for the energy dissipated during the impact [17].

For the foreign object impact, a strain rate above the range of 10^3 to 10^4 s⁻¹ is expected [8]. Thus, the strain rate becomes an important factor to consider regarding plastic behaviour. **So far the plastic behaviour of Ti-6Al-4V at very high strain rates, especially the hardening behaviour, is much less well understood. Therefore, an existing model [4] was employed in this work, which only consider the strain rate dependence of the yield stress. The ignorance of the rate-dependent hardening behaviour may have an effect on the initial residual stress field after the impact, however, this will not affect the stress relaxation behaviour under static cyclic loading, which is the main focus of this work.** Here the rate dependence is expressed in the power-law form [13]:

$$\dot{\epsilon} = \dot{\epsilon}_r \left(\frac{\sigma_{ys}(\dot{\epsilon})}{\sigma_{ys}} - 1 \right)^q \quad (3)$$

where $\dot{\epsilon}$ is the strain rate, $\sigma_{ys}(\dot{\epsilon})$ is the strain rate sensitive dynamic flow (yield) stress, σ_{ys} is the static flow stress (at $\dot{\epsilon} \approx 0$), and $\dot{\epsilon}_r$ and q are material constants. Note that the hardening behaviour is neglected by this material model, so that the results obtained from the impact modelling will not take into account the effects of hardening.

2.2 Material models for stress relaxation

In the literature the hardening behaviour of Ti-6Al-4V has been described by a number of material models. For example, the elastic-perfect plastic model has been used in ref [4] to predict residual stresses and deformation induced by a quasi-static indentation to Ti-6Al-4V. The same authors also suggested a non-linear kinematic model to take into account the Bauschinger effect, and the model was used to characterise residual stress relaxation from the quasi-static indentation [15]. In this study both material models are investigated to study the stress relaxation behaviour under cyclic fatigue loadings. Regarding a nonlinear kinematic hardening model, the translation of the centre of the yield surface in kinematic hardening is

governed by the back-stress tensor, \mathbf{x} , defined by the following equation (Ziegler kinematic hardening):

$$d\mathbf{x} = \frac{C}{\sigma_y}(\boldsymbol{\sigma} - \mathbf{x})d\mathbf{p} - \gamma\mathbf{x}d\mathbf{p} \quad (4)$$

where C and γ are material constants, σ_y is the yield surface size and $d\mathbf{p}$ is the increment in effective plastic strain, defined as:

$$d\mathbf{p} = \left(\frac{2}{3} d\boldsymbol{\varepsilon}^p : d\boldsymbol{\varepsilon}^p \right)^{\frac{1}{2}} \quad (5)$$

where the plastic strain increment, $d\boldsymbol{\varepsilon}^p$ is calculated via the flow rule, as follows:

$$d\boldsymbol{\varepsilon}^p = d\lambda \frac{\partial \mathbf{f}}{\partial \boldsymbol{\sigma}} = \frac{3}{2} d\mathbf{p} \frac{\boldsymbol{\sigma}'}{\sigma_e} \quad (6)$$

$$f = \sigma_e - \sigma_y = \left(\frac{3}{2} (\boldsymbol{\sigma}' - \mathbf{x}') : (\boldsymbol{\sigma}' - \mathbf{x}') \right)^{\frac{1}{2}} - \sigma_y \quad (7)$$

and f is the von Mises yield function, σ_e is the von Mises equivalent stress, $\boldsymbol{\sigma}'$ is the deviatoric stress tensor, \mathbf{x}' is the deviatoric back-stress tensor and $d\lambda$ is the plastic multiplier, which for a von Mises equivalent stress, is equal to the increment in effective plastic strain.

2.3 Modelling procedure

A hybrid explicit-implicit finite element modelling methodology was developed to simulate the foreign object impact and the subsequent stress relaxation due to cyclic fatigue loading, using a commercial FE code, ABAQUS [18]. The flowchart of the modelling procedure is illustrated in Fig. 1.

Foreign object impact on the plate is a highly dynamic event and is thus simulated using an explicit FE code. The explicit dynamics method was developed originally to simulate high speed dynamic events during which the load is applied rapidly and the response of the material and components changes rapidly. Explicit FE analysis is a powerful application of the explicit dynamic method whereby the problem is solved by analysing the motion of stress and deformation waves through the nodes of the structure using small time increments. ABAQUS/Explicit adopts a central difference rule to integrate the equations of motion explicitly through time, using the kinematic conditions at one increment to calculate the kinematic conditions at the next increment.

If only the explicit code was used, the stabilised stress state would take a long time to be reached due to a high frequency local numerical oscillation around the final result. In this study the deformed plate with all the transient stress and strain states was transferred from ABAQUS/Explicit to ABAQUS/Implicit after 10^{-4} s, to determine the residual stress field at static equilibrium. The transfer to the implicit code converts a final converging problem based on a small time increment into one based on Newtonian iteration, and removes all dynamic (inertia and damping) and boundary interaction forces. At the start of the analysis, the imported dynamic stress field was defined as the initial stress field. Artificial stresses of equal magnitude and opposite sign at each node point were then **automatically applied during the ABAQUS/implicit analysis**, resulting in their being zero internal forces. The artificial stresses were then removed linearly with respect to time, which allows the plate to deform further and a redistribution of the internal forces to occur. The final geometry and static stress field was

reached when the artificial forces were completely removed. When the stabilised residual stress was determined after dynamic impact, the deformed plate was loaded by the cyclic fatigue loading to capture the stress relaxation, still using ABAQUS/Implicit.

In this study the foreign object is simulated by a steel cube, impacting onto the centre of a flat plate. The notch takes a “V” shape in the specimen, representative of the “worst case” of indentation damage observed in aeroengine components [10,11]. Due to the symmetrical nature of the impact, only half of the plate and the foreign object are modelled. The FE model is shown in Fig. 2(a), in which the foreign object is modelled as a half-cube, impacting onto the centre of a flat half plate. For this case the half-width of the plate (along z direction) is 3mm, and the side length of the projector cube is 3mm. The FE model comprises over 45,000 eight-node linear brick elements with reduced integration. The mesh refinement detail at the impact site is shown in Fig. 2(b), showing that the mesh size near the contact region is $\leq 100 \mu\text{m}$. The mesh optimisation study has confirmed that this mesh density provides good convergence as well as reasonable computational cost. The loading cycles applied in the relaxation analyses are illustrated in Fig. 3.

The analysis is first carried out in ABAQUS/Explicit to simulate the foreign object impact normal to the plate, i.e. in the y -direction at a velocity of 200 m/s. 5. During the impact modelling, the bottom of the plate is constrained to not move in all three directions. The interaction between the cube and the plate surface is defined using the contact pair approach, which uses a master-slave algorithm to enforce the contact constraints, where the rigid surface of the cubic is chosen as the master contact surface. The friction between these surfaces is defined using the basic Coulomb friction model with isotropic friction and the friction coefficient is assumed to be 0.1. To avoid significant distortion of the elements induced by the impact, an Arbitrary Lagrangian Eulerian (ALE) adaptive meshing method is employed [18]. The plate specimens are made from rolled Ti-6Al-4V plate, the Young’s modulus and Possion’s ratio of which are 116 GPa and 0.34, respectively. The material constants used in Eq. (3) are followed those reported in ref [8], i.e. $\dot{\epsilon}_r$ is taken as $2 \times 10^{-4} \text{ s}^{-1}$ and n is taken as 3. σ_{ys} at $\dot{\epsilon} \approx 0$ is equal to 930 MPa.

The results obtained from the dynamic impact simulation are transferred to ABAQUS/Implicit to obtain the stabilised residual stresses after the impact (Step 1 as illustrated in Fig. 3). From Step 2 to Step 5 one end of the plate was loaded uniaxially in the x -direction, with a fixed boundary condition applied at the opposite end. This represents two fatigue cycles, as shown in Fig. 3, varying from a maximum applied stress σ_{\max} to a minimum one σ_{\min} . At the final step (Step 6), the applied stress is reduced to zero, giving the final residual stress field after the relaxation. Hence, the extent of stress relaxation is calculated as the difference between the residual stresses at Step 1 and Step 6. As mentioned earlier, the influence of the material behaviour on stress relaxation is studied based on two material models. For the nonlinear kinematic hardening model of Ti-6Al-4V, material constants C and γ in Eq. (4) are taken as 1.38×10^{11} and 635, respectively [15].

3 Results

3.1 Impact simulation

Fig. 4 shows a typical FE prediction for the foreign object damage. Note that the impact direction coincides with the y direction. A V-shape notch is predicted after impact, with plastic pile-up around the edges of the impact crater. Despite significant deformation associated with the impact simulation, the deformed mesh around the impact site has good quality by using adaptive meshing technique. Section views through the impact site are taken along the section line K-K’.

Fig. 5 shows the predicted contour of stabilised residual stresses, incurred by an impact velocity of 200 m/s (corresponding to the stress state at the end of load step 2). Fig. 5(a) shows two distinct σ_x stress concentrations: one is compressive directly beneath the impact site, the other is tensile around the outer edge of the impact. Figs. 5(b) and 5(c) show stress contours of σ_y and σ_z , respectively. All three stress components exhibit a similar compressive stress concentration, whilst their tensile stress distributions are significantly different.

The geometry of the plate has a dramatic influence on the impact-induced residual stress distribution. For example, Fig. 6 shows the predicted residual stress contour of σ_x when the half-width of the plate is reduced to 1mm, while the size of the projector is unchanged. The impact crater is approximately 1.5 mm in depth, more than twice that observed in the previous case. There is a small amount of plastic pile-up on the edges of the impact site and a prominent bulge protruding from the outer edge of the plate in the z-direction. Significant tensile stress concentrations are found on the edges of the notch, while a compressive stress concentration is found directly beneath the base of the notch. These results agree well with the simulations reported by Chen [8], which analysed a spherical impact projector.

3.2 Stress relaxation under cyclic loading

Experimental observations in [10,11] have clearly shown a mode I crack propagation behaviour from FOD, for which the crack grows along the plane normal to the x-direction (fatigue load direction). Therefore, in this work only the stress field and its relaxation in the x-direction are considered. The variation in the σ_x stress distribution with a fatigue loading, which is applied along the x direction in Fig. 2, is shown in Fig. 7. For this case the maximum applied load is 500 MPa with a stress ratio (R) of 0.01, and the material model used for the relaxation analysis is the elastic-perfectly plastic model. Under the maximum applied load, an increase in the compressive stress concentration from 1200 MPa to 2000 MPa is observed underneath the FOD impact, whilst the tensile stress concentrations around the edges of the impact are decreased by about 200 MPa (see Fig. 7(a)). Fig. 7(b) shows that the trend is reversed as the fatigue load is reduced to the minimum. Fig. 7 (c) shows the residual stress field after the removal of the fatigue loading. In comparison with the stress concentration after impact, as shown in Fig. 5(a), a re-distribution in the residual σ_x stress is clearly seen.

The material behaviour can have a significant effect on the local stress variation under the fatigue loading and the consequent stress relaxation. Fig. 8 shows the changes in σ_x with the fatigue loading for the positions P_1 and P_2 in Fig. 4. Here the maximum applied load is 500 MPa and the stress ratio R is 0.01. It is seen that for both locations, the non-linear hardening model leads to a higher mean stress magnitude than the perfectly-plastic model during the cyclic loading (steps 2 to 5), although the local stress range between the maximum and minimum applied loads remains the same for both material models. The stress level at the beginning of Step 2 is referred to as the initial residual stress after the impact, while the stress level at the end of Step 6 as the residual stress after the removal of the fatigue loading. Fig. 8 indicates that for a certain position in the tensile region (e.g. point P_1), the hardening model tends to increase the residual stress level, whilst the perfect plasticity model tends to decrease it. By contrast, both material models tend to reduce the residual stress level in the compressive region (e.g. point P_2). More details about the residual stress relaxation are given below.

3.3 Effects of stress ratio and maximum applied stress

The difference in the σ_x residual stresses between load steps 6 and 2 represents the magnitude of stress relaxation ($\Delta\sigma_r$) caused by the fatigue loading, or $\sigma_r = \sigma_{x,step6} - \sigma_{x,step2}$. The effects of stress ratio and the maximum applied stress on the local stress relaxation along the line DE

in the tensile residual stress region are given in Fig. 9. For a lower maximum load of 360 MPa, both hardening and perfect plasticity models cannot produce relaxation for the tensile stresses, but enhance the residual stress levels, giving positive values of $\Delta\sigma_r$. The increase is more evident with the non-linear hardening model with the largest value at Point D, i.e. close to the notch. With increasing distance from the notch, $\Delta\sigma_r$ decreases gradually. The perfect plasticity model also leads to a predicted increase in the residual stresses, but this increase is less than half that predicted by the hardening model, or about $0.05\sigma_{ys}$ (45MPa). For both material models the changes in $\Delta\sigma_r$ are independent of stress ratio.

For a σ_{max} of 500 MPa, the hardening model still predicts similar results to those of $\sigma_{max} = 360$ MPa. For the perfect plasticity model, however, predicted negative $\Delta\sigma_r$ values indicate the relaxation of tensile residual stresses, except for positions close to the impact, e.g. point D. Again the changes in $\Delta\sigma_r$ are not influenced by the stress ratio, for either plasticity model.

The effects of stress ratio and maximum stress on the residual stress relaxation along line BA is shown in Fig. 10. The residual compressive stresses are seen to relax for both maximum applied stresses. The perfect plasticity model induces more relaxation than the hardening model, but the stress ratio has no effect on the relaxation. The largest relaxation is seen to be close to the base of the impact notch, e.g. about 0.4 mm from point B, and then the relaxation decreases as the distance from the notch increases.

Due to the existence of residual stresses and stress concentrations induced by the FOD impact, the local stress ratio R_{local} will be different from the applied stress ratio R . Fig. 11 shows the effects of the applied stress ratio and maximum stress on R_{local} along the line DE in the tensile residual stress zone. For $R = 0.01$, the local load ratio is about 0.25 at the edge of the impact notch (near Point D), and increases to about 0.6 towards the boundary of the plate (Point E). In addition, R_{local} is a slightly higher for the hardening model than that for the perfect plasticity model. This may be attributed to the fact that the hardening model leads to a higher mean stress under the cyclic fatigue loading, although the stress range during the cycle remains the same for both material models, e.g. see Fig. 8.

4. Discussion

A previous study in [10] has shown that a finite element methodology, similar to that presented here, can successfully predict the size of the impact damage, which gives confidence in the material model (i.e. Eq. (3)) used for the impact modeling. In addition, the study also suggested a two-parameter crack growth model to correlate fatigue crack growth data from FOD, in which the effects of stress concentration and residual stress incurred by FOD was incorporated by the El Haddad small-crack theory [19]. However, the relaxation of residual stresses under cyclic fatigue loading was not considered in [10]. In the present study this issue is addressed by a hybrid explicit-implicit finite element approach, which allows the transition from a rate dependent material model (for dynamic impact modelling) to a cyclic hardening material model (for static stress analysis). **It is important to note that ABAQUS/Explicit only can be used to determine the final residual stress field from FOD (e.g. as reported in [4]). The impact simulation conducted in this study showed that for the FE model in Fig. 2, the cube bounces back in 5×10^{-6} s, when the maximum transient stresses are observed within the plate. However, the response of the target material will take much longer to become stabilised owing to the reflection and interaction of various stress waves produced in the target material. Accurate tracking of the front of various stress waves is important to capture the dynamic response of the material. The explicit algorithm is especially well-suited to solving this high-speed dynamic event efficiently. On the other hand, the high-speed dynamic deformation processes tend to generate a large amount of elastic strain energy in the material. The elastic strain energy, which has been stored in the material after performing the explicit dynamic analysis, is subsequently released. In this case the stabilised residual**

stress field is obtained when the solution time of the explicit analysis is run about 1×10^{-3} s, but this analysis is extremely time costly, especially between 1×10^{-4} s to 1×10^{-3} s. The hybrid explicit-implicit method is thereby employed here to facilitate rapid convergence, which is used to release all the elastic strain energy efficiently and to obtain the final stabilised residual stress field. In this study, the explicit analysis is stopped 1×10^{-4} s and this transient stress state is read into ABAQUS/implicit. The stabilised residual stresses, predicted by the explicit analysis only and hybrid explicit-implicit analysis, have been compared, and the difference between them was found to be negligible.

Two distinct types of behaviour of residual stress relaxation are predicted around the FOD site. For the compressive residual area immediately beneath the impact, stress relaxation is predicted irrespective of the maximum stress applied (Fig. 10). This means that the compressive stress is reduced by the cyclic loading. For the residual tensile stress area, by contrast, an increase in the residual stress is predicted, especially for hardening material model (Fig. 9). In addition, both figures show that the change of the stress ratio from 0.01 to 0.7 has no influence on the residual stress relaxation. It is important to note that limited analyses were also performed for a negative R-value ($R = -1$), and the preliminary results show the effects of (negative) R ratio on the stress relaxation, in comparison with the positive R ratio. However, the details of stress relaxation under fully reversed loading condition are not typical for crack growth behaviours from FOD under in-service aeroengine loading conditions, and thereby will be address elsewhere. On the other hand, the maximum stress can significantly affect the stress relaxation for the compressive region, whilst it seems to have negligible effect for the tensile region when it changes from 360 MPa to 500 MPa. These results suggest that the compressive residual stresses tend to relax more significantly due to the applied tensile stress than the tensile residual stresses. The level of tensile residual stresses after FOD is about 350 ~ 500 MP and this is increased by the tensile fatigue loading. The increase can be attributed to the compensation in the residual relaxation under the compressive region.

Significantly higher local stress ratios are predicted for the tensile area than the applied stress ratios, as illustrated in Fig. 11. This may be an important reason why crack growth rates from FOD are higher than those obtained from long crack growth data under the corresponding applied stress ratios, as observed from experimental work [9,10].

For future study, one important issue is to experimentally measure the residual stress relaxation after FOD to validate the present model. Boyce et al. [3] has reported both experimental and numerical results on the relaxation of residual stresses induced by a static indentation. Compared with the indentation, the dynamic impact or FOD induces more significant residual stresses and deformation. Also, FOD may generate microcracks and change the local strength of the targeted material. The importance of those issues needs to be addressed via experimental investigation of residual stress relaxation. In addition, this study has been focused on the impact and the subsequent stress relaxation of a 3mm plate. The impact analysis of a thinner plate has shown the different distribution of residual stresses, giving an indication of possible dimension/FOD size effect. Therefore, it is very necessary to include parametric analyses in the further, such as the effect of plate thickness, the impact angle and the shape of the projector.

5. Summary

The relaxation of the residual stresses associated with a cubic impact onto a plate of Ti-6Al-4V has been predicted using a finite element approach. The main conclusions are drawn as follows:

1. Relaxation and redistribution of the residual stresses occurs during the cyclic loading. The σ_x compressive stresses tend to relax, whilst the tensile stresses tend to increase,

creating a preferential region for crack initiation and growth. This is predominantly seen under a non-linear kinematic hardening material model.

2. The non-linear kinematic hardening model gives a different material response under cyclic loading than the perfect plasticity model. It decreases the relaxation of the compressive stress concentration but increases the magnitude of the tensile stress concentration.
3. The relaxation of the residual stresses is dependent on the applied maximum stress, but is largely independent of **positive** stress ratio for both material models.
4. Along the tensile region (e.g. line DE), the local stress ratio R_{local} is greater than the applied ratio, which will promote fatigue crack growth from FOD.

Acknowledgements

The authors would like to thank the Nuffield Foundation for the research grant awarded to T. Davis for this study.

References

1. Ritchie R.O., Davidson D.L., Boyce B.L., Campbell J.P., Roder O. High-cycle fatigue of Ti-6Al-4V. *Fatigue and Fracture Engineering of Materials and Structures*, 1999, 22, 621-631.
2. Ritchie R.O., Boyce B.L., Campbell J.P., Roder O., Thompson A.W., Milligan W.W. Thresholds for high-cycle fatigue in a turbine engine Ti-6Al-4V alloy. *International Journal of Fatigue*, 1999, 21(7), 653-662.
3. Boyce B.L., Chen X., Peters J.O., Hutchinson J.W., Ritchie R.O. Mechanical relaxation of localized residual stresses associated with foreign object damage. *Materials Science and Engineering A*, 2003, A349, 48-58.
4. Boyce B.L., Chen X., Hutchinson J.W., Ritchie R.O. The residual stress state due to a spherical hard-body impact. *Mechanics of Materials*, 2001, 33, 441-454.
5. Ruschau J., Thompson S.R., Nicholas T. High cycle fatigue limit stresses for airfoils subjected to foreign object damage. *International Journal of Fatigue*, 2003, 25, 955-962.
6. Peters J.O., Ritchie R.O. Foreign-object damage and high-cycle fatigue: role of microstructure in Ti-6Al-4V. *International Journal of Fatigue*, 2001, 23, 413-421.
7. Peters J.O., Ritchie R.O., Chen X., McNaney J.M., Hutchinson J.W., Ritchie R.O. On the application of the Kitagawa-Takahashi diagram to foreign-object damage and high-cycle fatigue. *Engineering Fracture Mechanics*, 2002, 69, 1425-1446.
8. Chen X. Foreign object damage on the leading edge of a thin blade. *Mechanics of Materials*, 2005, 37, 447-457.
9. Ding J., Hall R.F., Byrne J., Tong J. Fatigue Crack Growth from foreign object damage under combined low and high cycle loading. Part I: Experimental studies. *International Journal of Fatigue*, 2007, 29, 1339-1349.
10. Ding J., Hall R.F., Byrne J., Tong J. Fatigue Crack Growth from foreign object damage under combined low and high cycle loading. Part II: A two-parameter predictive approach. *International Journal of Fatigue*, 2007, 29, 1339-1349.
11. Duó P., Liu J., Dini D., Golshan M., Korunsky A. M. Evaluation of residual stresses due to foreign object damage. *Mechanics of Materials*, 2007, 39, 199-211.
12. Chen X., Hutchinson J.W. Foreign object damage and fatigue notch threshold: Cracking outside shallow indents. *International Journal of Fracture*, 2001, 107, 31-51.
13. Chen X., Hutchinson J.W. Particle impact on metal substrates with application to foreign object damage to aircraft engines. *Journal of Mechanics and Physics of Solids*, 2002, 50, 2669-2690.
14. Torres M.A.S., Voorwald H.J.C. An evaluation of shot peening, residual stress and stress relaxation on the fatigue life of AISI 4340 steel. *International Journal of Fatigue*, 2002, 24, 877-866.

15. Boyce B.L., Chen X., Peters J.O., Hutchinson J.W., Ritchie R.O. Mechanical relaxation of localized residual stresses associated with foreign object damage. *Materials Science and Engineering A*, 2003, A349, 48-58.
16. Frija M., Hassine T., Fathallah R., Bouraoui C., Dogui A. Finite element modelling of the shot peening process: Prediction of the compressive residual stresses, the plastic deformations and the surface integrity. *Materials Science and Engineering A*, 2006, 426, 173-180.
17. Johnson W. *Impact Strength of Materials*. Edward Arnold, London, 1972,
18. ABAQUS User's Manual, Version 6.6. Hibbitt, Karlsson and Sorenson, Inc, 2006.
19. El Haddad M.H., Topper T.H. and Smith K.N. Prediction of non propagating cracks, *Eng Fract Mech*, 1979, 11, 573–584.

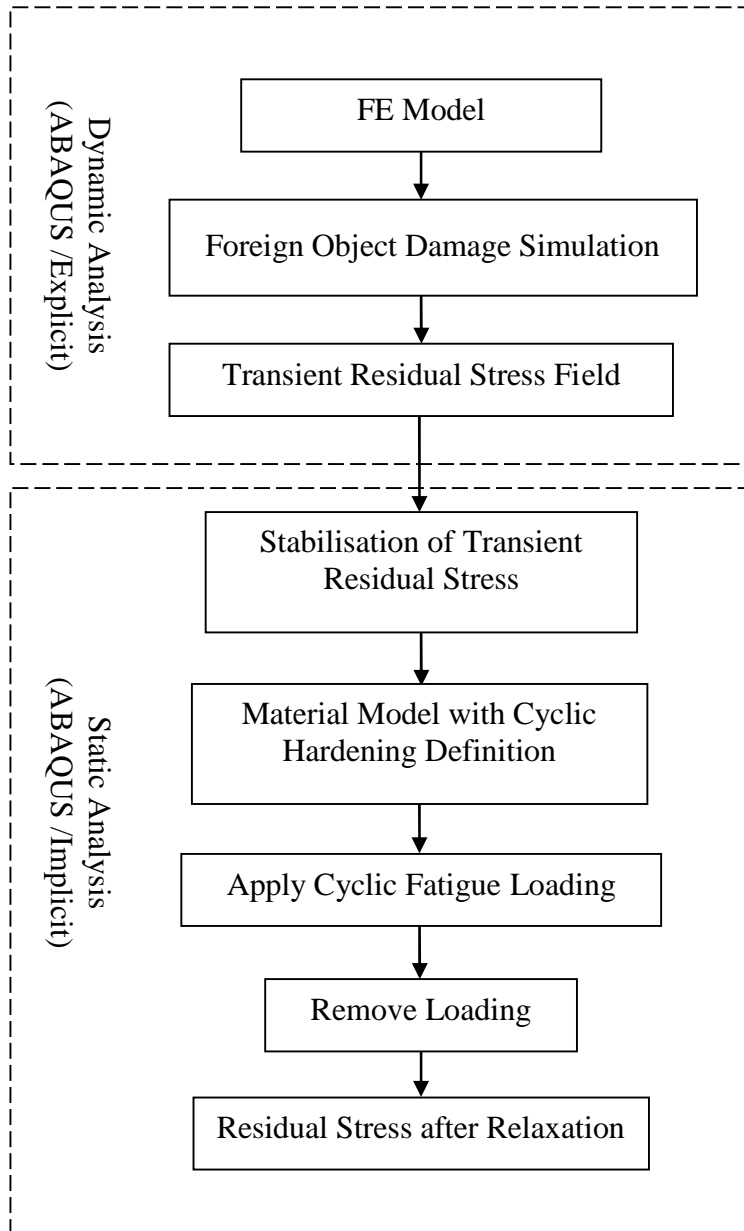


Fig. 1 Flowchart of the hybrid explicit/implicit finite element methodology to determine the residual stress relaxation after foreign object damage.

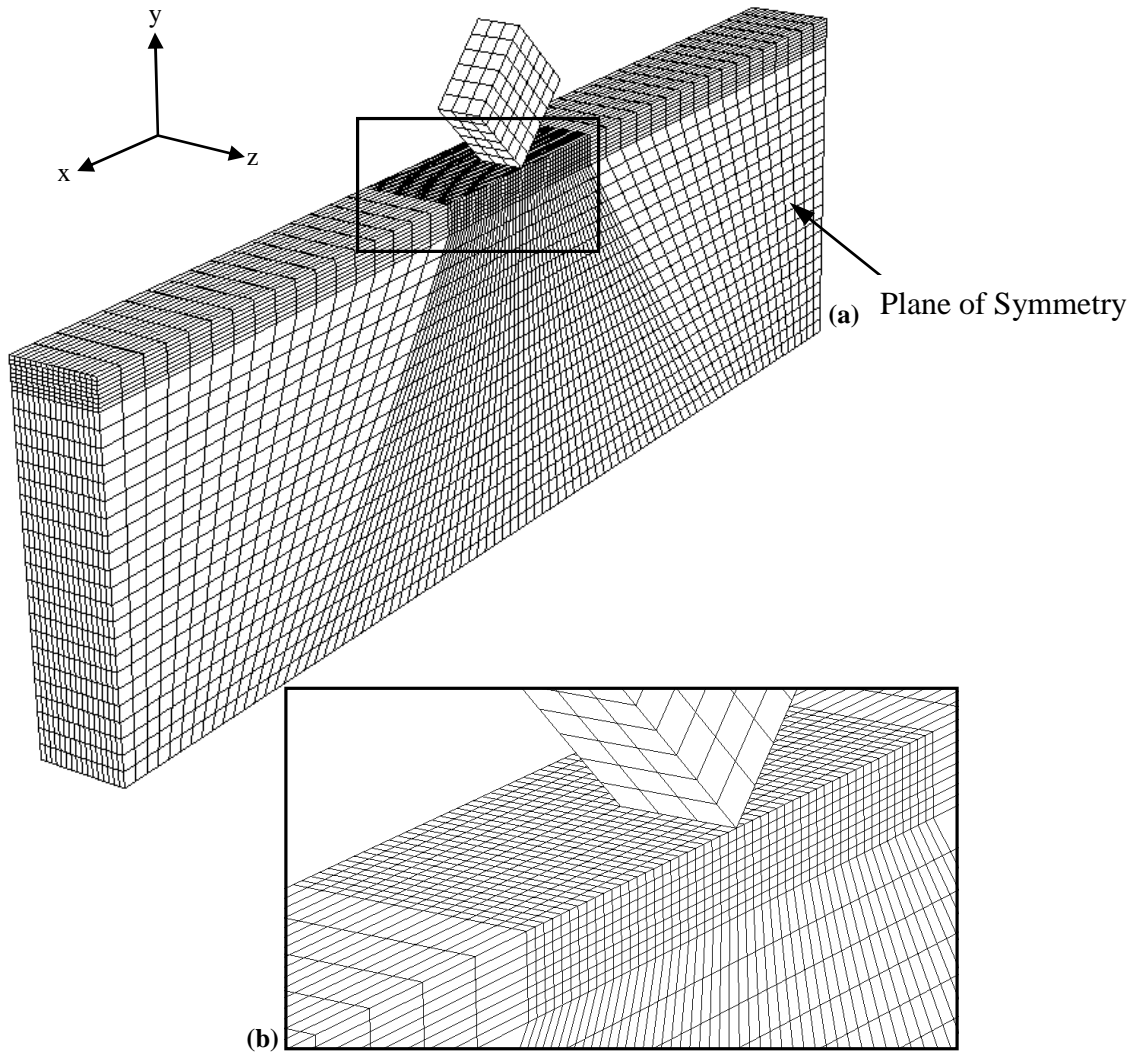


Fig. 2 (a) FE model of the cube impacting onto a flat plate and (b) detailed view of dense mesh at foreign object impact site.

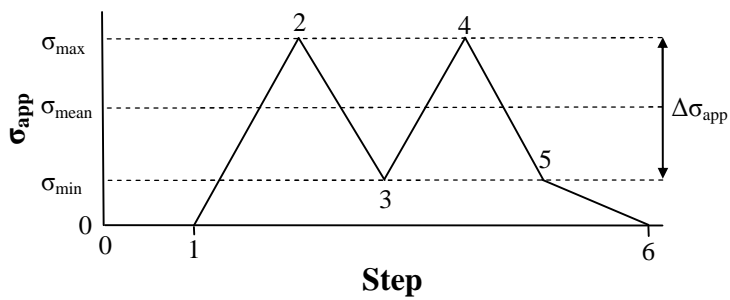


Fig. 3 Applied cyclic fatigue loading for the stress relaxation analyses.

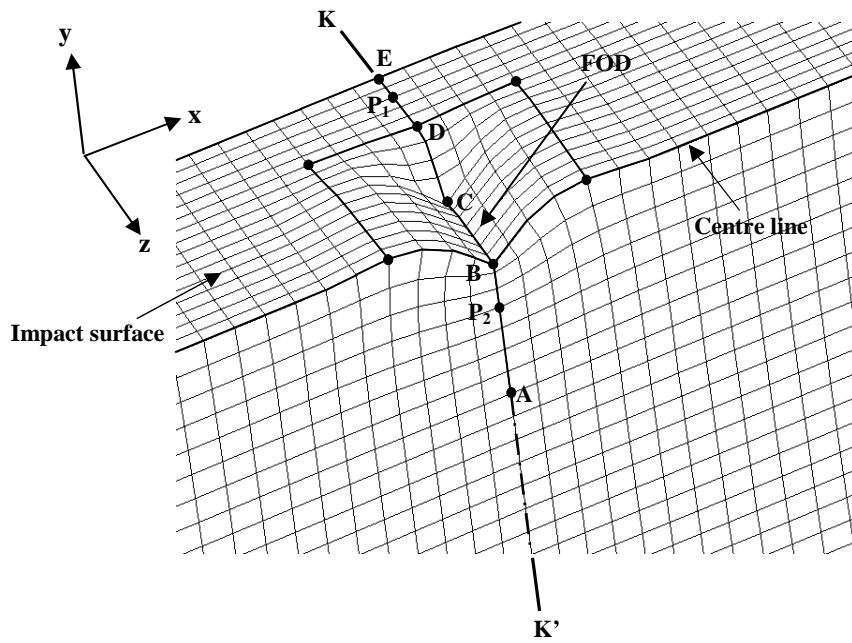
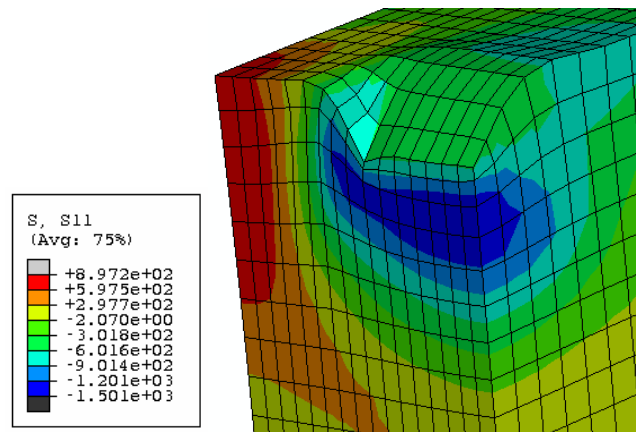
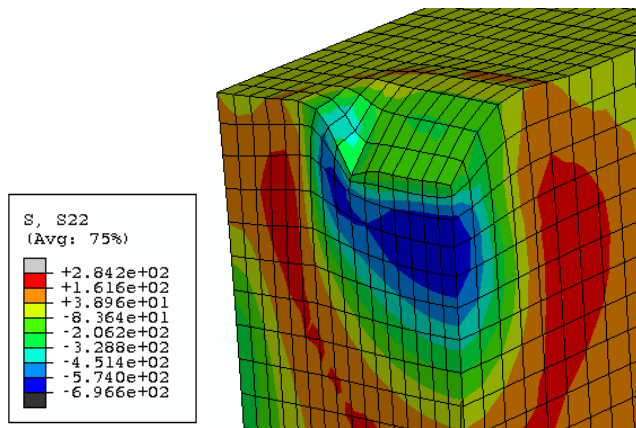


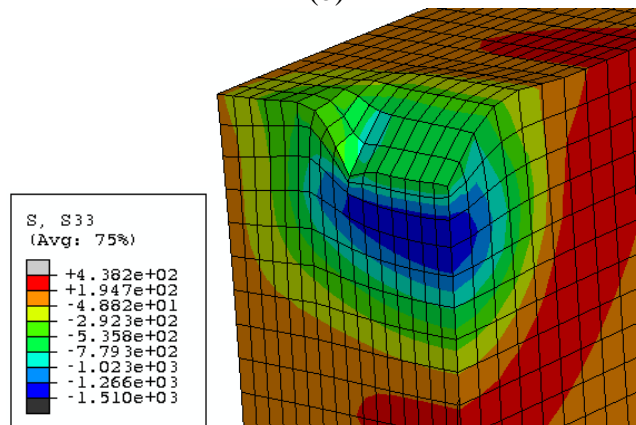
Fig. 4 Schematic of foreign object damage with direction of the stress components in the x , y and z directions and the section line $K-K'$.



(a)



(b)



(c)

Fig. 5 Contours of the stabilised residual stress field after the FOD: (a) the σ_x stress field; (b) the σ_y stress field and (c) the σ_z stress field.

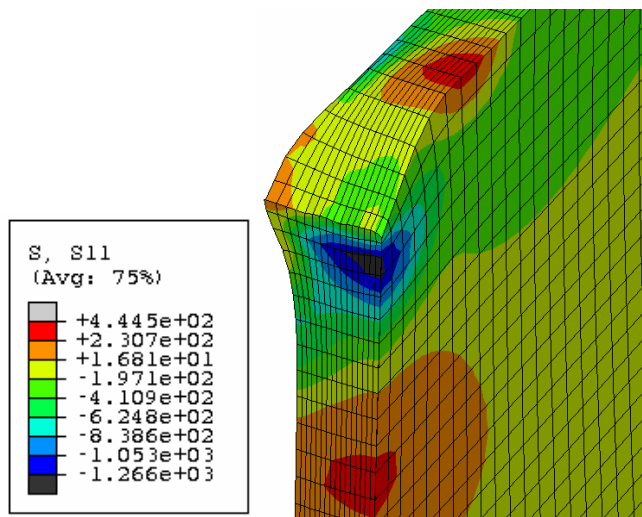
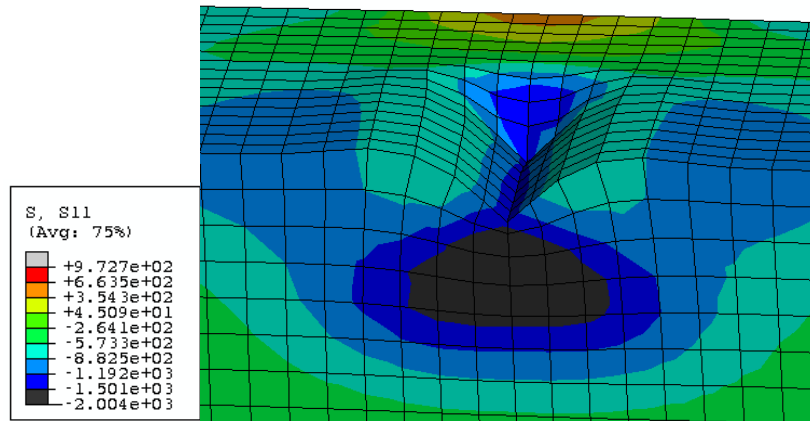
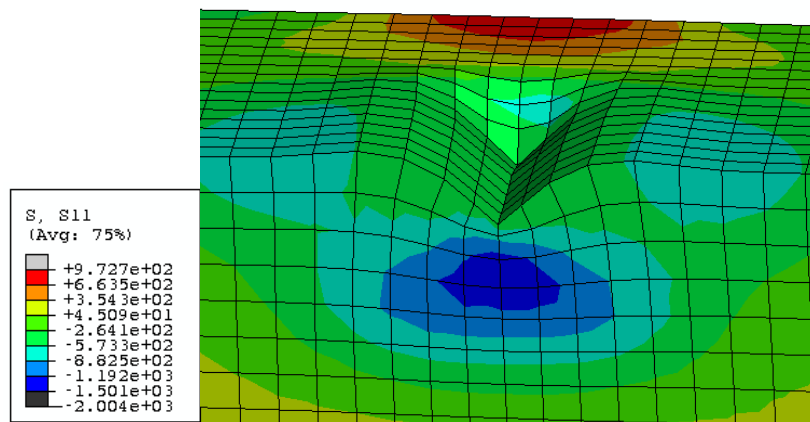


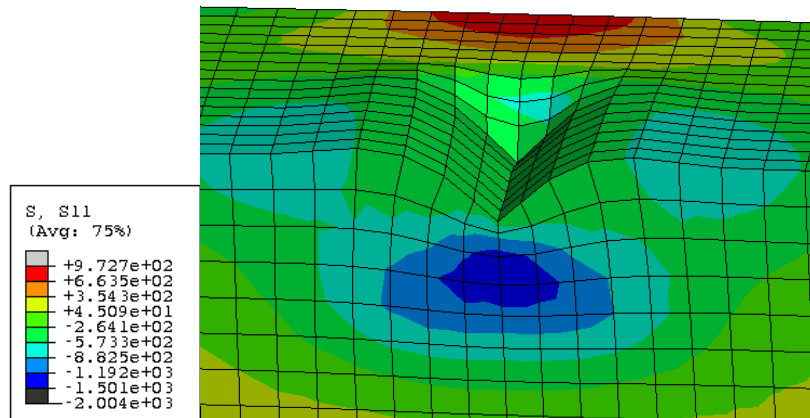
Fig. 6 Contour of the stabilised σ_x residual stress field after the FOD for a thin plate.



(a)



(b)



(c)

Fig. 7 Predicted variation of the σ_x stress field contour under a cyclic fatigue loading with a stress ratio of 0.01: (a) $\sigma_{app} = 500$ MPa; (b) $\sigma_{app} = 5$ MPa and (c) the residual stress after relaxation ($\sigma_{app} = 0$ MPa).

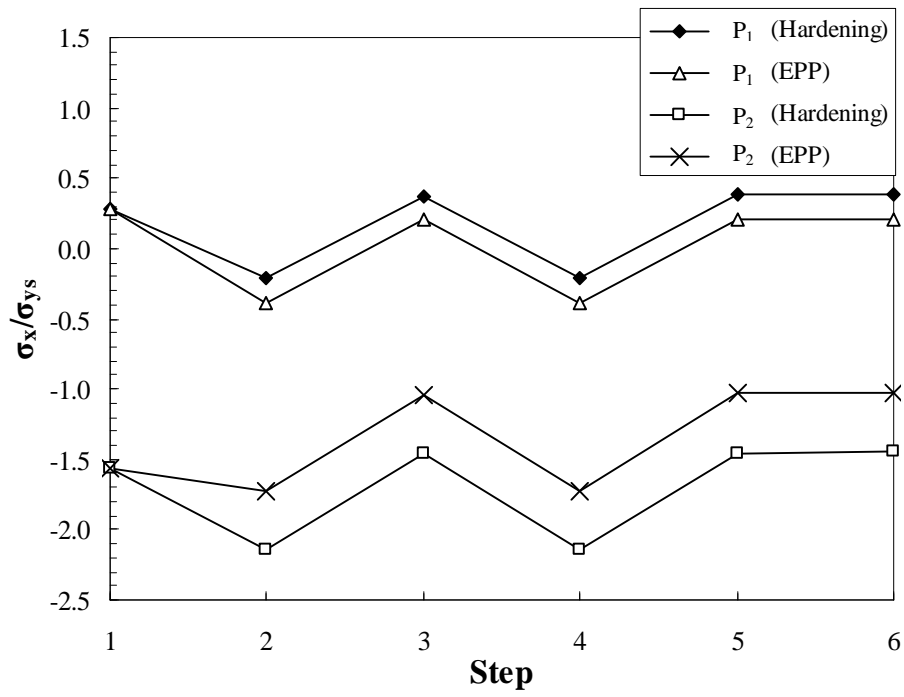
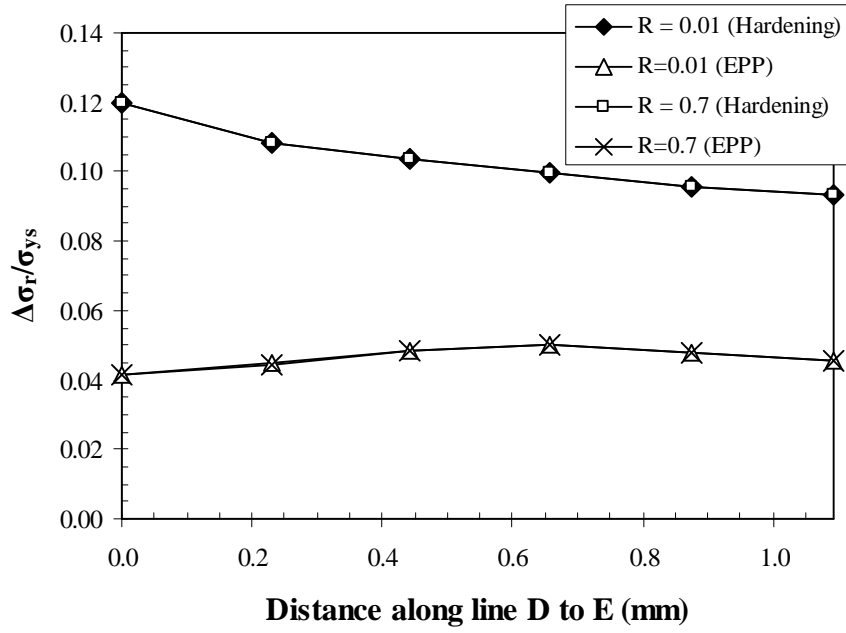
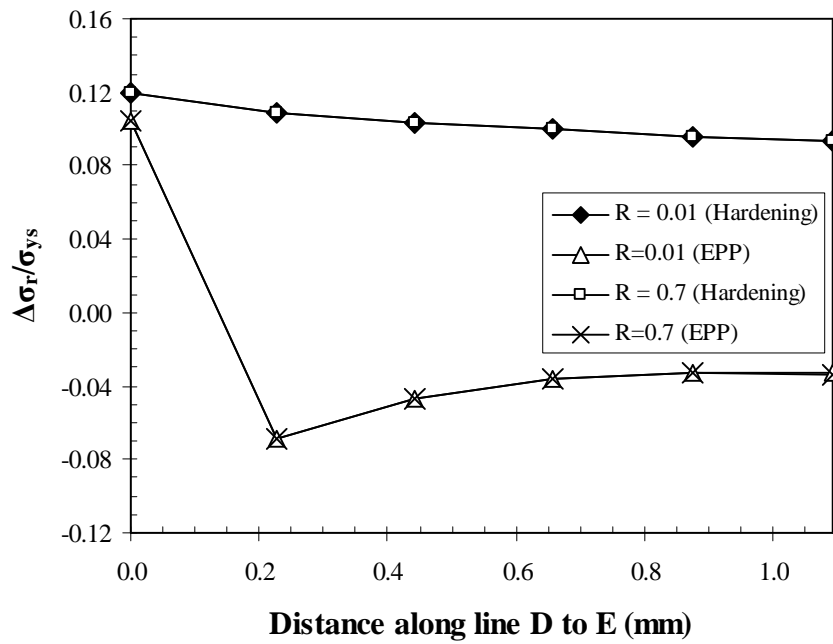


Fig. 8 Predicted evolution of the σ_x stress at points P1 and P2 (see Fig. 4) over load steps 1 to 6. EPP – Elastic-perfect plasticity model; Hardening – Non-linear kinematic hardening model.

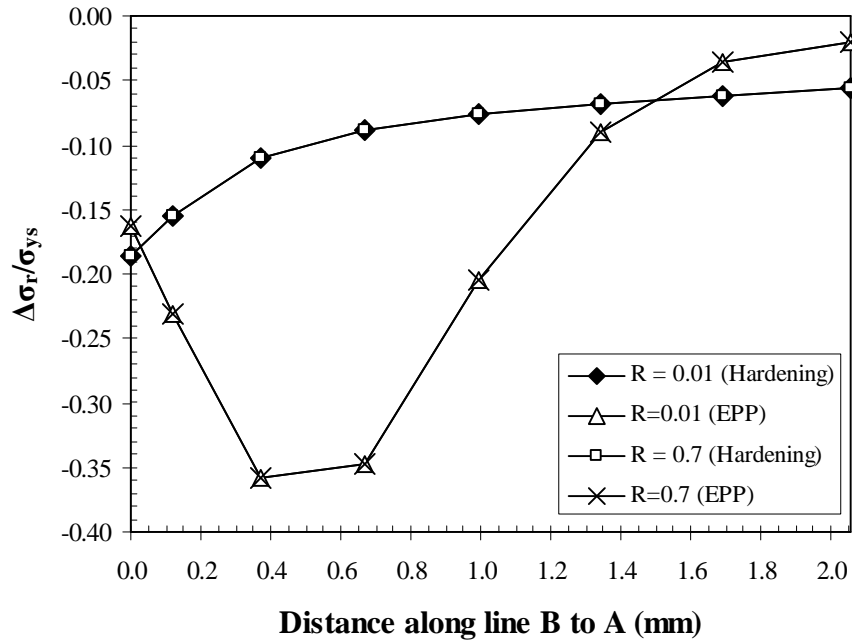


(a)

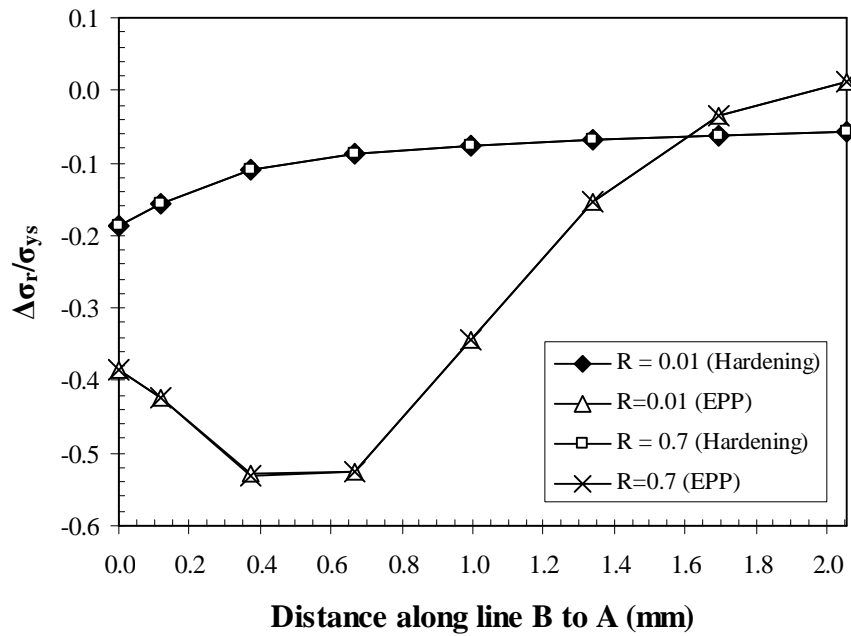


(b)

Fig. 9 Normalised stress σ_r relaxation along the line DE in Fig. 4 for: (a) $\sigma_{\max} = 360$ MPa; and (b) $\sigma_{\max} = 500$. EPP – Elastic-perfect plasticity model; Hardening – Non-linear kinematic hardening model.



(a)



(b)

Fig. 10 Normalised stress σ_r relaxation along the line AB in Fig. 4 for: (a) $\sigma_{\max} = 360$ MPa; and (b) $\sigma_{\max} = 500$. EPP – Elastic-perfect plasticity model; Hardening – Non-linear kinematic hardening model.

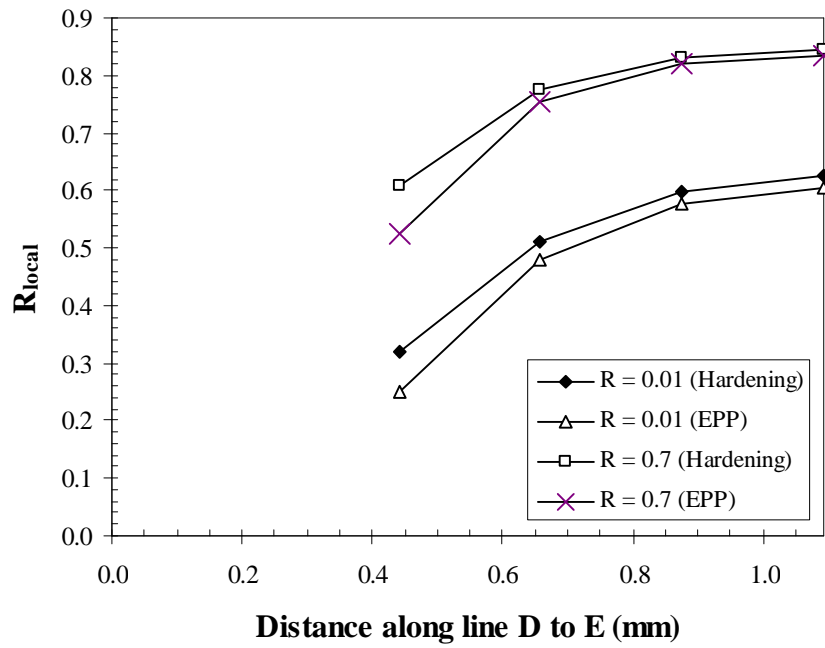


Fig. 11 Predicted stress ratio for σ_x stress along the DE in Fig. 4 under a maximum applied stress of 360 MPa. EPP – Elastic-perfect plasticity model; Hardening – Non-linear kinematic hardening model..